Supplementary Materials for EPAPS: Fluctuation-Dissipation Theorem in an Isolated System of Quantum Dipolar Bosons after a Quench

Ehsan Khatami,[1] Guido Pupillo,[2] Mark Srednicki,[3] and Marcos Rigol[4]

[1]*Department of Physics, University of California, Santa Cruz, California 95064, USA*
[2]*IPCMS (UMR 7504) and ISIS (UMR 7006), Université de Strasbourg and CNRS, Strasbourg, France*
[3]*Department of Physics, University of California, Santa Barbara, California 93106, USA*
[4]*Department of Physics, The Pennsylvania State University, University Park, Pennsylvania 16802, USA*

EXPERIMENTAL RELEVANCE OF OUR MODEL

Hamiltonian (1) in the main text provides a microscopic description for the dynamics of a gas of bosonic ground state molecules such as, e.g., LiCs molecules (dipole moment $d_{\max} \approx 5.6$ Debye), confined transversely (longitudinally) by a two-dimensional (one-dimensional) optical lattice with frequency $\omega_\perp$ ($\omega_\parallel$), with $\omega_\perp \gg \omega_\parallel$. The molecules are polarized in the transverse direction by an external electric field of strength F and are confined to the lowest band of the 1D lattice, provided $\omega_\parallel > \max\{V,J,T\}$. Here, $V = d^2/(4\pi\varepsilon_0 a_\parallel^3)$, with $d \lesssim d_{\max}$ the dipole moment induced by F, $a_\parallel$ the lattice spacing in 1D and ε_0 the vacuum permittivity. The hard-core condition is obtained by requiring that molecules are trapped with a low-density n, such that the initial system has no doubly occupied sites [1]. The additional condition $n^{-1/2} \gg (d_{\max}^2/\hbar\omega_\parallel)^{1/3} \simeq 360$nm ensures collisional stability [1]. The model in Eq. (1) of the main text can also describe the dynamics of a gas of strongly magnetic atoms such as Dy (dipole moment $d = 10\mu_B$, with μ_B Bohr's magneton) or Er ($d = 7\mu_B$). In this case, the hard-core constraint is achieved by means of magnetic tuning of the short-range scattering length using Feshbach resonances [2], while J/V decreases exponentially with increasing the depth of the 1D lattice [3].

THERMALIZATION

Despite the presence of interactions that have a power-law decay with distance, we find that the behavior of eigenstate expectation values of few-body observables, as well as thermalization properties of the systems described by Hamiltonian (1) of the main text, are qualitatively similar to those already seen in models with short-range (nearest and next-nearest-neighbor) interactions [4, 5].

In order to show that this is indeed the case, here we study the difference between the results of the diagonal ensemble for the few-body observables studied in main text, namely, n_j and n_k, as well as for the density-density structure factor, N_k (not studied in the main text), and the results of the microcanonical ensemble. The momentum distribution function and the density-density structure factor are defined as

$$\hat{n}_k = \frac{1}{L}\sum_{l,m} e^{ik(l-m)}\hat{b}_l^\dagger \hat{b}_m, \quad \hat{N}_k = \frac{1}{L}\sum_{l,m} e^{ik(l-m)}\hat{n}_l\hat{n}_m. \qquad (1)$$

They are the Fourier transforms of the one-particle and density-density correlation matrices, respectively. Since we work at fixed number of particles, $\langle N_{k=0}\rangle = p^2/L$, so we set it to zero without any loss of generality. These observables can be studied in ultracold gases experiments.

We define the microcanonical average for an observable $\hat{O}$ as $O_{\rm micro} = \frac{1}{\mathcal{N}_{\Delta E}}\sum_\alpha O_{\alpha\alpha}$. Here, $\mathcal{N}_{\Delta E}$ is the number of states in the microcanonical window, which is centered around $E_{\rm tot}$ and has a width of ΔE [6]. We average the results over several close values of ΔE for each system size to ensure that they are robust against small changes in ΔE. The values for ΔE are in $[0.2-0.25]$ for $L=12$, and $[0.1-0.15]$ for $L=15$ and 18.

We compute the normalized difference between the predictions of the diagonal and the microcanonical ensembles,

$$\Delta O = \frac{\sum_\ell |O_{\rm diag}(\ell) - O_{\rm micro}(\ell)|}{\sum_l O_{\rm diag}(\ell)}, \qquad (2)$$

where ℓ stands for either the site index or the momentum index depending of the observable.

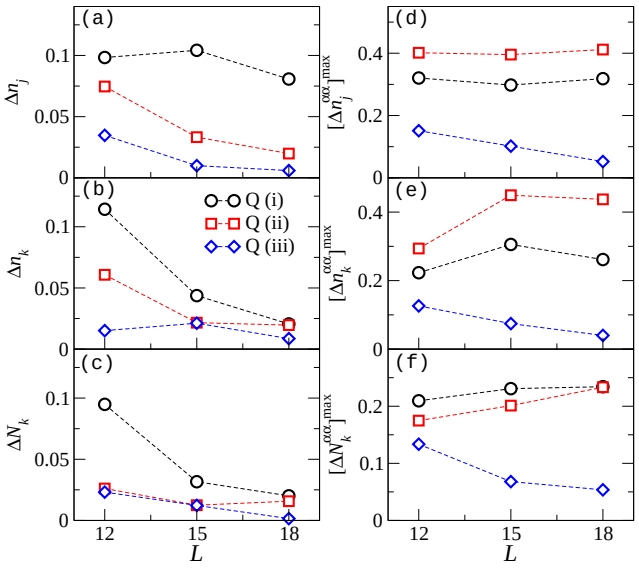

FIG. 1. (a)-(c) Normalized differences between the diagonal and microcanonical ensemble averages for the three observables, n_j, n_k, and N_k [see Eq. (2)] vs L. Different plots in each panel correspond to the three quench types [identified by Q (i), Q (ii), and Q (iii)]. (d)-(f) Maximum of the normalized differences between the microcanonical average and each of the eigenstate expectation values in the microcanonical energy window [see Eq. (3)] vs L.

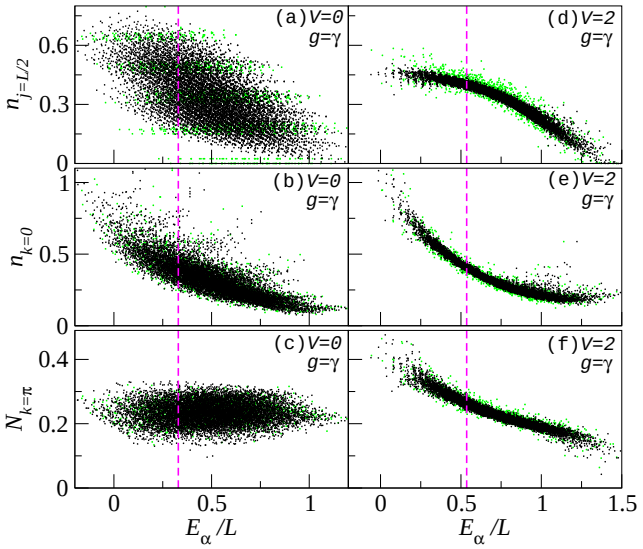

FIG. 2. Eigenstate expectation values values of $\hat{n}_{j=L/2}$, $\hat{n}_{k=0}$, and $\hat{N}_{k=\pi}$ over the entire spectrum vs the scaled eigenenergies for the noninteracting (a)-(c), and interacting system (d)-(f). We show results for $L=15$ as the green (light colored) points, and for $L=18$ as the black (dark) ones in each panel. The vertical lines show the location of $E_{\rm tot}/L$ for $L=18$, which is also roughly equal to that of $L=15$.

In Fig. 1(a)–(c), we show results for ΔO vs L for the three types of quenches described in the main text. We find that for quench type (i) (between two integrable systems), ΔO is generally larger in comparison to ΔO for the other two quenches, and that this feature remains apparent as the system size increases to $L=18$. Previous studies, involving the same integrable model without [7–9] and with [8] the trapping potential and much larger system sizes, have found strong indications that ΔO (where O was either the density or the momentum distribution function) remains finite in the thermodynamic limit so that the system does not thermalize. On the other hand, trends for quench type (iii) suggest that the differences vanish by increasing the system size, i.e., that the nonintegrable dipolar system thermalizes in the thermodynamic limit. The trend is less clear for quench type (ii) as we see that Δn_j monotonically decreases by increasing L, whereas Δn_k and ΔN_k appear to saturate by increasing L from $L=15$ to $L=18$. Clearly, larger system sizes are required to confirm whether thermalization takes place for such an integrable system after a quench from a nonintegrable one as argued in Ref. [10].

As mentioned in the main text, for a generic (nonintegrable) system, thermalization can be understood through the ETH. Here, we examine the validity of the ETH for each case considered by calculating the normalized differences between the observable in each eigenstate and the microcanonical average,

$$\Delta O_{\alpha\alpha} = \frac{\sum_l |O_{\alpha\alpha}(l) - O_{\rm micro}(l)|}{\sum_l O_{\rm micro}(l)}, \qquad (3)$$

and taking the maximal difference within the microcanonical window, $[\Delta O^{\alpha\alpha}]^{\rm max} = {\rm Max}[\Delta O_{\alpha\alpha}]_{\Delta E}$. This is a measure of how widely the eigenstate expectation values are spread in the microcanonical window. In Fig. 1(d)-1(f), we show this quantity for our three observables vs L. They are seen to consistently decrease with increasing system size for the final Hamiltonian in quench type (iii) while they are seem to saturate to relatively large values for the final Hamiltonians in quenches type (i) and type (ii). This is an indication that eigenstate thermalization occurs in the former case while it fails in the latter ones.

The validity, or failure, of ETH can be perhaps more easily seen by plotting the eigenstate expectation value of observables vs the eigenenergies, as shown in Fig. 2. For the integrable system with $V=0$ [Fig. 2(a)-2(c)], eigenstate expectation values exhibit large fluctuations inside the microcanonical energy window for both $L=15$ and 18, and the width of the region where the values are scattered around $E_{\rm tot}$ does not decrease with increasing the system size, i.e., eigenstate thermalization does not occur. This is different from what happens in the nonintegrable case [Fig. 2(d)-2(f)], where each of the eigenstate expectation values of an observable inside a narrow energy window around $E_{\rm tot}$ approaches the microcanonical average as the system size is increased. This is apparent as the width of the region where the values reside around $E_{\rm tot}$ decreases with increasing system size, and presumably vanishes in the thermodynamic limit.

ENERGY SCALES

The short-time evolution of the correlation functions is set by the width of $f(E,\omega)$ as a function of ω, which we denote as W. Note that, as discussed in the main text, f is not well defined for integrable systems and, even for the nonintegrable case for which Eq. (3) of the main text is seen to better describe the data as the system size increases, one cannot disentangle f from the random function $R_{\alpha\beta}$ with merely the knowledge of the off-diagonal values. Therefore, we estimate W for another closely related function, $f_{\rm cg}(\omega)$, which is obtained by coarse-graining the off-diagonal values. We then calculate the width using

$$W = \frac{2\int_0^\infty |f_{\rm cg}(\omega)|^2 d\omega}{|f_{\rm cg}(0)|^2}. \qquad (4)$$

Examples of $f_{\rm cg}(\omega)$ are depicted as lines in the right panels of Fig. 4. We choose different bin sizes for different systems. They are, $50\times\delta$ for $L=12$, $300\times\delta$ for $L=15$, and $700\times\delta$ for $L=18$, where δ is the average level spacing.

In Fig. 3(a)-3(c), we plot W versus L in the three quenches and for the three observables considered. For $n_{j=L/2}$ and $n_{k=0}$, W varies non-monotonically with L in most cases, while for $N_{k=\pi}$, it is seen to monotonically decrease with increasing L and possibly saturate to a finite value for larger system sizes. Larger system sizes are needed to understand the behavior of W in macroscopic systems. Regardless, the values obtained here can be used in each case to estimate the time scale for the initial decrease of the fluctuation or dissipation correlation functions.

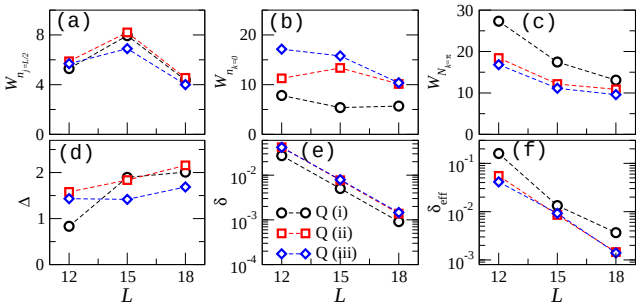

FIG. 3. Various energy scales in the model vs L. Top panels show the estimates for the width of the off-diagonal function, $f(E,\omega)$ in the ω space. (d) shows the uncertainty in the total energy, and (e)-(f) show the average level spacings (see text).

In Fig. 3(d), we also show the quantum uncertainty of the energy, Δ. We find that they are $\mathcal{O}(10^0)$ for the systems studied here, and increase slowly with system size, as expected from the analysis in Ref. [11].

The time scale for recurrences in the correlation functions is set by the average level spacing, δ (estimated by $e^{S(E)}E$ [12]), which, as expected, is found to decrease exponentially with increasing the system size from $\mathcal{O}(10^{-1})$ for $L=12$ to $\mathcal{O}(10^{-3})$ for $L=18$ [see Fig. 3(e)]. Therefore, such a time scale for typical system sizes explored in experiments would be much too large to have any relevance. This is also true if one calculates $\delta_{\rm eff}$ $(=\frac{\Delta}{\sum_\alpha |c_\alpha|^4})$ [12], shown in Fig. 3(f), which represents the effective level spacing between the eigenstates participating in the diagonal ensemble.

OTHER OBSERVABLES AND/OR SYSTEM SIZE

In the main text, we show the fluctuation and dissipation correlation functions of $n_{j=L/2}$ for the two largest system sizes, $L=15$ and 18. For completeness, in Fig. 4, we show the same quantities, as well as the corresponding off-diagonal elements of the two observables shown in Fig. 3 of the main text, for the smallest system we have studied, $L=12$. Because of the smaller size of the Hilbert space in comparison to the other clusters, some of the trends seen in Fig. 1 of the main text are not so clear in the case of $L=12$. However, the suppression in the fluctuations of the correlation functions for the nonintegrable case [Fig. 4(c)] is apparent in the corresponding histogram. Other features, such as the dramatic change in the behavior of the off-diagonal elements of $n_{j=L/2}$ when the integrability-breaking interaction is introduced, is already seen in Figs. 4(d)-4(f) for this small cluster.

In Fig. 5, we show the histograms of the differences between $C_{\rm Fluc}(t)$ and $C_{\rm Diss}(t)$, and between $C_{\rm Fluc}(t)$ and $C_{\rm Appr}(t)$ for the three quench types studied in the main text and for the two largest system sizes accessible to us. The results in this figure complement those of the normalized variances presented in Fig. 2 of the main text. Figures 5(a) and 5(b) show that, in quenches type (i), there are no signatures of a reduction with

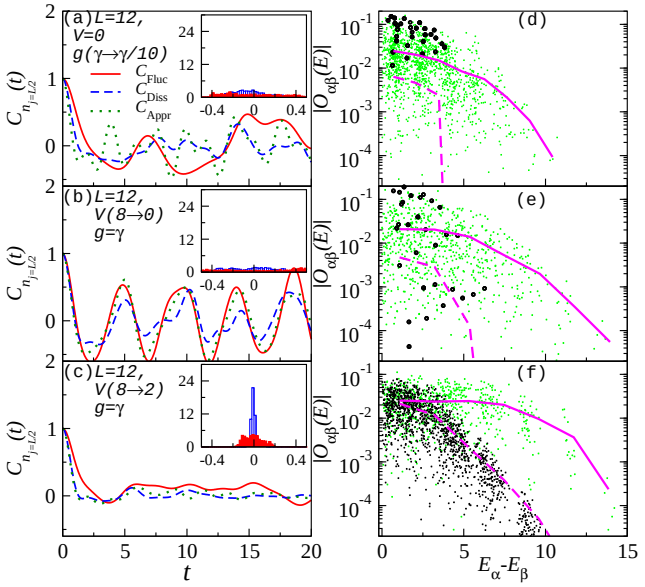

FIG. 4. Left panels (Right panels): the same as Fig. 1 (Fig. 3) of the main text, except that $L=12$, and that the lines in the right panels are coarse-grained functions of the off-diagonal values used to calculate the width of data in ω using Eq. (4). In the right panels, solid (dashed) lines correspond to $n_{k=0}$ ($n_{j=L/2}$). The bin size for coarse-graining is $50\times\delta$ for this system size.

increasing system size of the large differences seen between the different correlation functions at each given time (Fig. 1 of the main text). A similar conclusion stands for the behavior of $C_{\rm Fluc}(t)-C_{\rm Appr}(t)$ in quenches type (ii) [Fig. 5(d)]. On the other hand, the histograms of $C_{\rm Fluc}(t)-C_{\rm Diss}(t)$ in quenches type (ii) [Fig. 5(c)], and of $C_{\rm Fluc}(t)-C_{\rm Diss}(t)$ as well as $C_{\rm Fluc}(t)-C_{\rm Appr}(t)$ in quenches type (iii) [Fig. 5(e) and 5(f), respectively] make apparent than not only does the variances decrease with increasing system size as shown in Fig. 1 of the main text, but also the maximal differences between the correlation functions at each given time decrease with increasing system size.

In Figs. 6 and 7, we show results for the fluctuation and dissipation correlation functions of $n_{k=0}$ and $N_{k=\pi}$ for the three system sizes and quench types considered in the main text. The contrast between the results for different quenches can be seen to be similar to the one in Fig. 1 of the main text for $n_{j=L/2}$. The main difference between the results for $n_{k=0}$ and $N_{k=\pi}$ when compared to those for $n_{j=L/2}$ is that the former two exhibit smaller fluctuations with increasing system size than the latter one. This is to be expected as the presence of the harmonic trap, which breaks translational symmetry, produces a larger number of nonzero off-diagonal matrix elements of $n_{k=0}$ and $N_{k=\pi}$ in the integrable regime than of $n_{j=L/2}$ (see Fig. 3 of the main text). Still, those fluctuations [see the histograms in the insets of Figs. 6(a)–6(f) and Figs. 7(a)–7(f)] can be seen to be much stronger than in the nonintegrable case [see the histograms in the insets in Figs. 6(g)–6(i) and Figs. 7(g)–7(i)].

The results for the scaling of the variances between

$C_{\rm Fluc}(t) - C_{\rm Diss}(t)$ and $C_{\rm Fluc}(t) - C_{\rm Appr}(t)$ for $n_{k=0}$ and $N_{k=\pi}$ are presented in Fig. 8. They are also consistent with the conclusions extracted from the scaling of those differences for $n_{j=L/2}$.

Finally, in Fig. 9, we show results for the off-diagonal matrix elements of $N_{k=\pi}$ within ΔE of $E_{\rm tot}$. Those results are the equivalent of the ones presented in Fig. 3 of the main text for $n_{j=L/2}$ and $n_{k=0}$. That figure shows that the conclusions drawn for the latter two observables in the main text are also applicable to $N_{k=\pi}$.

[1] H. Büchler, A. Micheli, and P. Zoller, Nature Phys. **3**, 726 (2007).

[2] M. Berninger, A. Zenesini, B. Huang, W. Harm, H.-C. Nägerl, F. Ferlaino, R. Grimm, P. S. Julienne, and J. M. Hutson, arXiv:1212.5584 (2012).

[3] I. Bloch, J. Dalibard, and W. Zwerger, Rev. Mod. Phys. **80**, 885 (2008).

[4] M. Rigol, Phys. Rev. Lett. **103**, 100403 (2009); Phys. Rev. A **80**, 053607 (2009); L. F. Santos and M. Rigol, Phys. Rev. E **81**, 036206 (2010); *ibid* **82**, 031130 (2010).

[5] C. Neuenhahn and F. Marquardt, Phys. Rev. E **85**, 060101 (2012).

[6] For details, see the Supplimentary Materials of Ref. [11].

[7] M. Rigol, V. Dunjko, V. Yurovsky, and M. Olshanii, Phys. Rev. Lett. **98**, 050405 (2007).

[8] M. Rigol, A. Muramatsu, and M. Olshanii, Phys. Rev. A **74**, 053616 (2006).

[9] A. C. Cassidy, C. W. Clark, and M. Rigol, Phys. Rev. Lett. **106**, 140405 (2011).

[10] M. Rigol and M. Srednicki, Phys. Rev. Lett. **108**, 110601 (2012); K. He and M. Rigol, Phys. Rev. A **87**, 043615 (2013).

[11] M. Rigol, V. Dunjko, and M. Olshanii, Nature **452**, 854 (2008).

[12] M. Srednicki, J. Phys. A **32**, 1163 (1999).

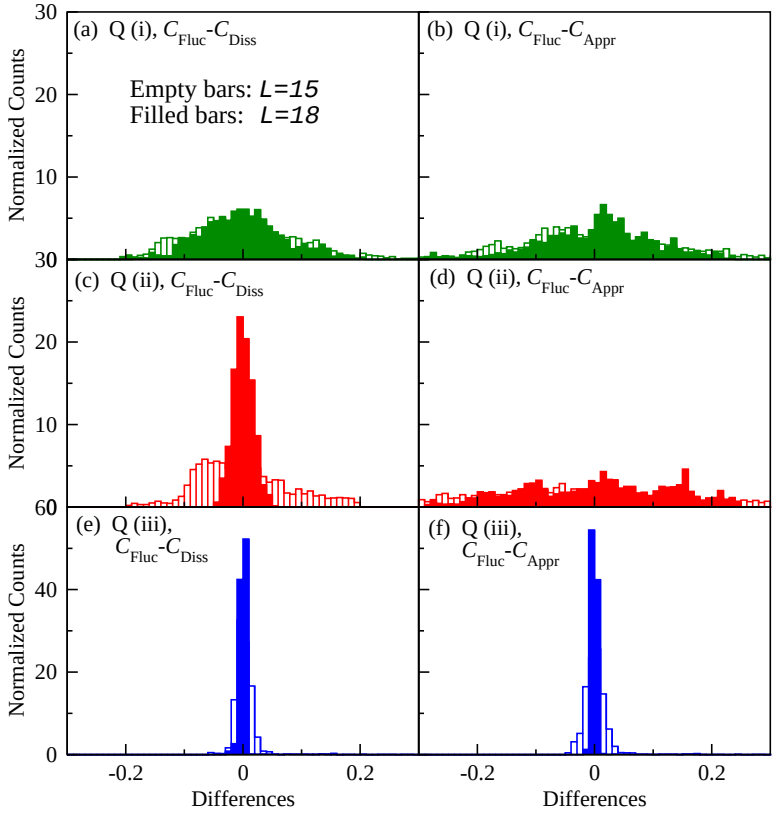

FIG. 5. Normalized histograms of $C_{\rm Fluc}(t) - C_{\rm Diss}(t)$ (left panels) and $C_{\rm Fluc}(t) - C_{\rm Appr}(t)$ (right panels) for $n_{j=L/2}$, and for the three quenches (from top to bottom) and the two largest system sizes, calculated for 2000 data points between $t = 0$ and 100.

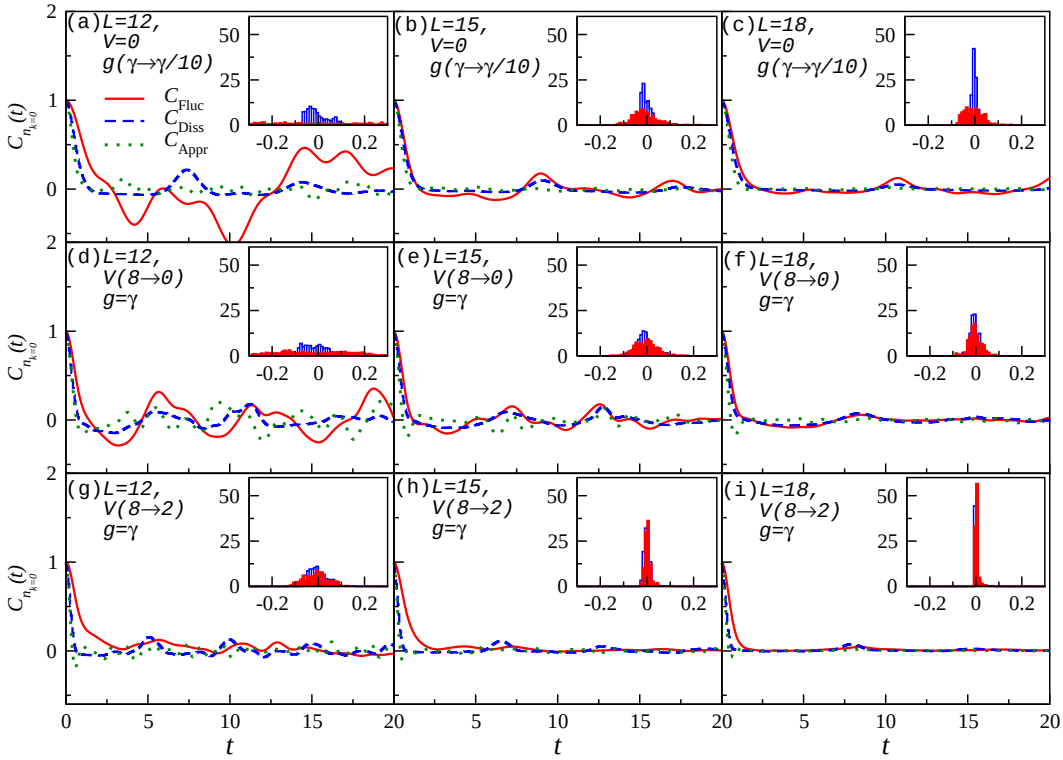

FIG. 6. The same as Fig. 1 of the main text, except that here, the observable is the zero-momentum occupation number, $n_{k=0}$. We have also included the results for $L = 12$ in the left panels.

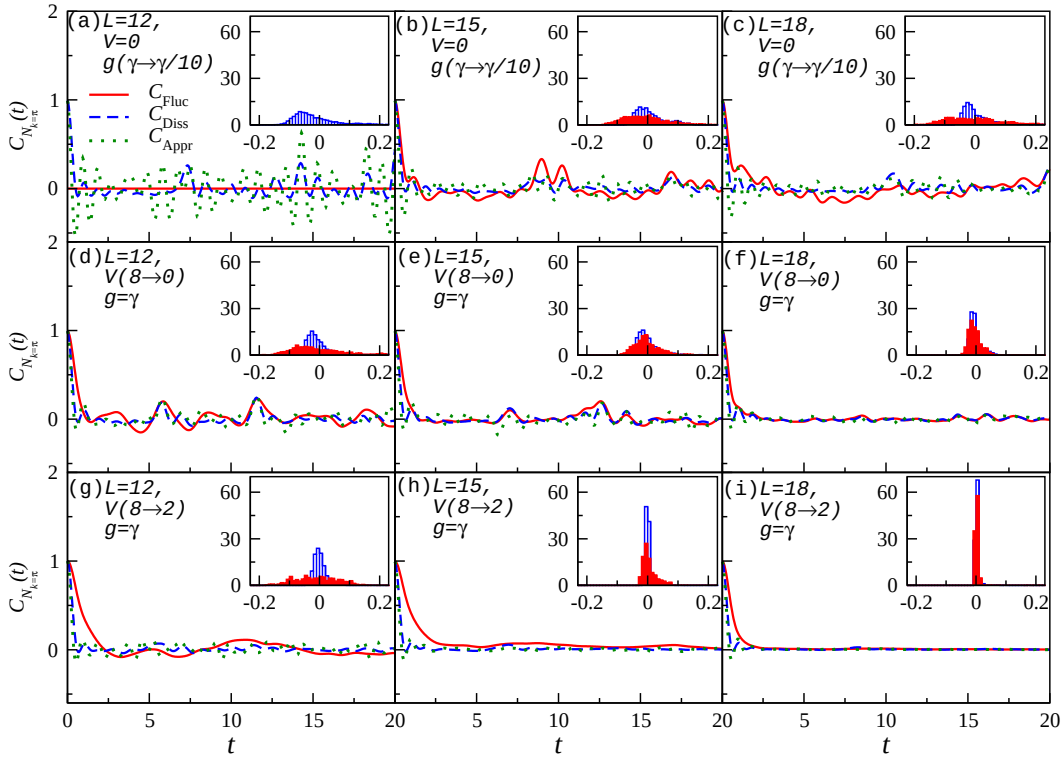

FIG. 7. The same as Fig. 1 of the main text, except that here, the observable is the $k = \pi$ density-density structure factor, $N_{k=\pi}$. We have also included the results for $L = 12$ in the left panels. For quench type (i), we find that the value of $N_{k=\pi}$ for $L = 12$ does not exhibit any dynamics. This is reflected in the corresponding fluctuation correlation function in (a), which is zero at all times. For this reason, we have set $C_{\rm Fluc}(t) = 0$ in that case and are not showing its histogram. This is unique to $N_{k=\pi}$ for $L = 12$ and to the specific parameters chosen for quench type (i).

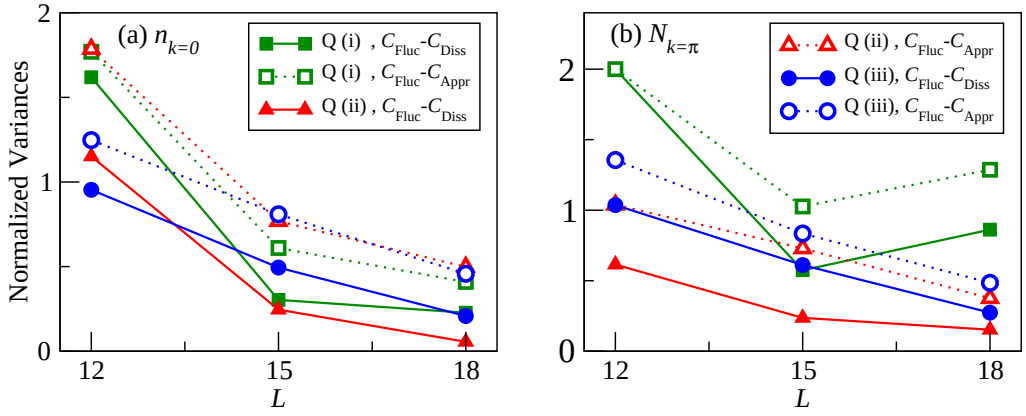

FIG. 8. Same as Fig. 2 of the main text, but for when the observables are $n_{k=0}$ (a), and $N_{k=\pi}$ (b).

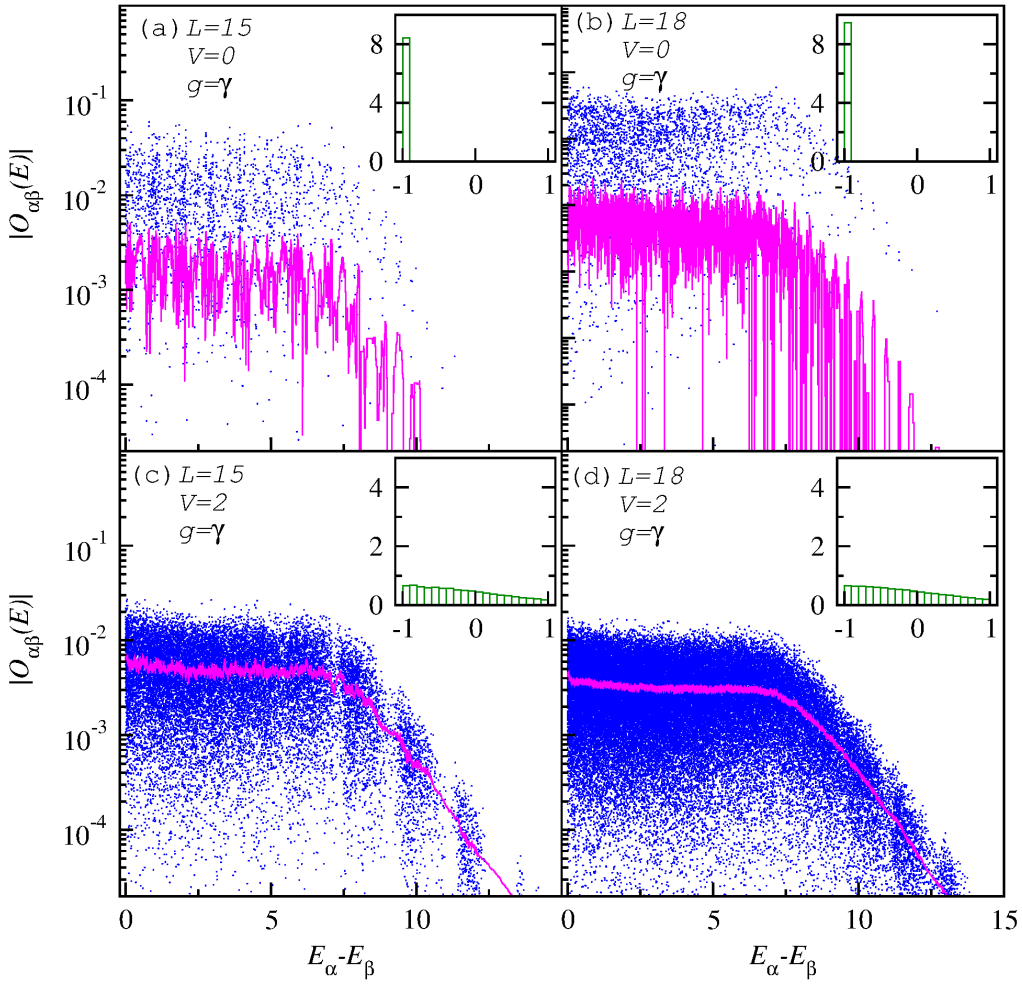

FIG. 9. Same as Fig. 3 of the main text, but for when the observable is $N_{k=\pi}$. Here, we show all the data points in all of the cases. Lines are running averages with a subset length of 100 for $L = 15$ and 1000 for $L = 18$.